The MOSS camera on H-1NF

C. A. Michael,[a] J. Howard, and B. D. Blackwell
Plasma Research Laboratory, Research School of Physical Sciences and Engineering, Australian National University, Canberra A.C.T. 0200, Australia

(Presented on 21 June 2000)

We have configured the modulated optical solid-state spectrometer, a recently developed high-resolution instrument for plasma Doppler spectroscopy, as an imaging spectroscopic camera. The camera features a wide field of view (~10°), large aperture (40 mm), and high spectral resolution $\nu/\Delta\nu$ greater than 10 000. The camera installation on the H-1NF Heliac is described, together with the steps in the design process, including field widening. Calibration and characterization of the instrument function is discussed and the instrument performance is illustrated with some sample results of spatially resolved ion temperature measurements in H-1NF. © *2001 American Institute of Physics.* [DOI: 10.1063/1.1326903]

I. INTRODUCTION

The modulated optical solid-state (MOSS) spectrometer[1,2] has recently been developed for high-resolution Doppler and polarization spectroscopy of plasmas. The camera is a multichannel version of this instrument and has been used for routine measurements of ion flow speed and temperature from Doppler broadening of transition radiation in the H-1 Heliac, a three period helical axis stellarator, at the Australian National University (ANU).[3]

Using standard 50 mm camera lenses, the multichannel MOSS camera images the entire poloidal cross section of the H-1 plasma onto a linear array of 16 photomultiplier detectors. Because all the spectral information is encoded in the temporal frequency domain, only a single light detector per spatial channel is required. This opens the possibility to perform truly two-dimensional (2D) spectral imaging. The imaging system which brackets the spectrometer (see Figs. 1 and 2), consists of an objective lens that collects and colimates rays emanating from the source and a final camera lens that forms the image of the source on the detector array. The temperature and light intensity profiles, $T(\rho)$ and $I(\rho)$, where ρ is the flux surface coordinate, can be unfolded from the line-averaged measurements under the assumption that flux surfaces are isotherms and have constant emissivity.[4]

One of the benefits of Fourier-transform spectrometers, such as the MOSS spectrometer, over wave front division instruments such as a grating spectrometer, is the fact that, for a given spectral resolution, the optical throughput is much larger because the entrance aperture is not limited by an entrance slit (the Jaquinot Advantage[5,6]). Field-of-view (FOV) limitations on the collected light solid angle can be overcome using field-widening techniques. In particular, interferometers based on polarizing optics can obtain significant advantage using fairly straightforward optical strategies. (see Fig. 4).

Because of its high light throughput and attendant temporal resolution, the camera can be used to infer the ion thermal diffusivity by modulating the plasma heating source and measuring the spatial profile of corresponding modulations in ion temperature.[7]

II. MEASUREMENT PRINCIPLE OF THE MOSS SPECTROMETER

The light intensity at the detector, for a two-beam interferometer (such as MOSS), is given by

$$I = \frac{I_0}{2}(1 + \zeta \cos\phi), \tag{1}$$

where I_0 is the source intensity, ζ is the fringe visibility or contrast, and ϕ is the phase retardation of the interferometer. The MOSS spectrometer is a modulated, fixed delay interferometer which introduces a phase shift $\phi = \phi_0 + \phi_1 \cos(2\pi\Omega t)$, where $\phi_1 \sim \pi/2$ and $\phi_0 \gg \phi_1$. The sinusoidal modulation of the interferometer phase generates harmonic components at the modulation frequency. The relative intensities of the odd and even harmonic components can be numerically extracted to obtain time-resolved estimates of the average light intensity, the offset phase ϕ_0, and contrast ζ. Assuming that the distribution function is Maxwellian, these quantities are related to the emission-weighted species flow speed V_s and temperature T_s.[8] Ignoring line-integration effects, we have

$$\phi_0 = \phi_I\left(1 + \frac{V_s}{c}\right), \qquad \zeta = \zeta_I \zeta_S, \quad \zeta_S = e^{-(T_s/T_c)}. \tag{2}$$

The instrumental phase ϕ_I and contrast ζ_I depend on the light collection geometry. They may be understood by analogy with the instrument function for a grating spectrometer. The phase calibration ϕ_I corresponds to the wavelength calibration: phase shifts due to the Doppler effect are measured with respect to this value. The instrument contrast represents a false measurement of line broadening, which is due to admitting a finite solid angle of rays to the detector. It is similar

[a]Author to whom correspondence should be addressed; electronic mail: clive.michael@anu.edu.au

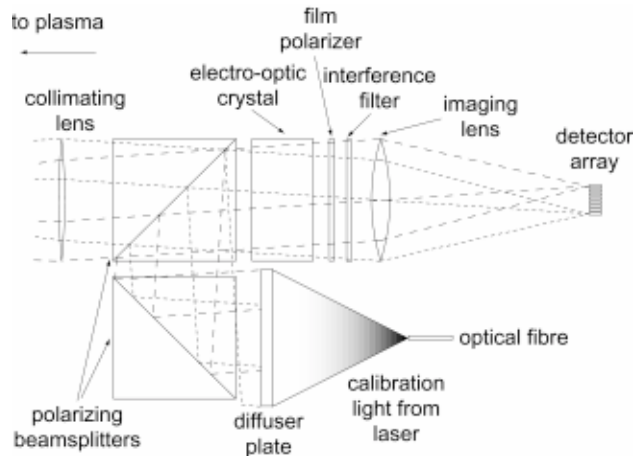

FIG. 1. Close-up view of the camera, showing the calibration system and ray paths demonstrating the imaging principle.

to the slit function for a grating spectrometer. The quantity T_c is the temperature at which the instrument is most sensitive, and is related to the spectral resolving power and in turn, the crystal length. This is analogous to the grating dispersion. In order that the measured contrast ζ and phase ϕ be most sensitive to changes in temperature and flow speed, the instrument contrast should be as close to unity as possible.

III. FOV

When imaging an extended light source, each detector element receives rays that have traversed the spectrometer over a range of incidence angles. This therefore results in a spread in the path length delay through the interferometer that can reduce the overall fringe contrast and so compromise the signal-to-noise ratio.

The phase variation with angle is

$$\phi(\theta,\eta)=2\pi\frac{L}{\cos\theta}\frac{B(\theta,\eta)}{\lambda}, \tag{3}$$

where θ is the angle of incidence and η is the azimuth with respect to the optic axis of the birefringent crystal. For a Michelson interferometer, $B=1$ and the resulting fringe pattern is circular. However, for a uniaxial birefringent crystal, the birefringence is a function of angle,[9,10] and for small θ the phase is

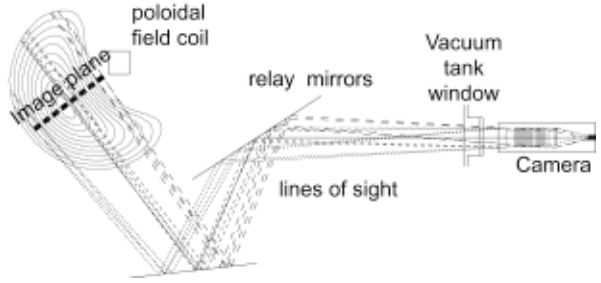

FIG. 2. The optical arrangement of the MOSS camera located on the H-1NF Heliac.

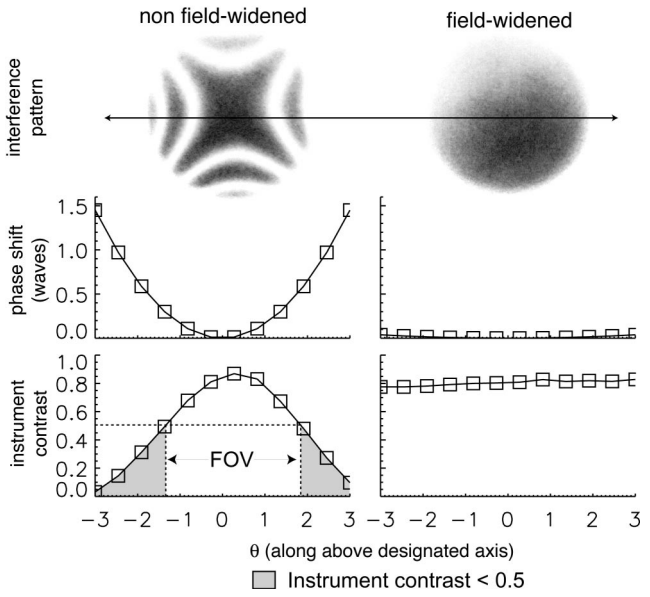

FIG. 3. Comparison of the between interference pattern, phase, and contrast variation with angle between a nonfield widened and a field widened system. The photograph of interference pattern in the image plane was taken using laser calibration light. The field widened system was 2×15 mm crystals; the nonfield widened system was a 25 mm crystal.

$$\phi(\theta,\eta)=2\pi\frac{LB_0}{\lambda}\left(1+\frac{\theta^2}{2n_0}\left(\frac{\cos^2\eta}{n_e}-\frac{\sin^2\eta}{n_0}\right)\right). \tag{4}$$

The function $\phi(\theta,\eta)$ has a saddle point at the origin. The magnitude of the increase in phase along the axis $\eta=0$ almost exactly balances the decrease along $\eta=90°$, because n_0 is close to n_e. The associated fringes are therefore hyperbolic in shape (see Fig. 3).

Because the phase change is quadratically dependent on θ, detector elements centered further off axis will gather rays which have a larger range of phase shifts, thereby resulting in a lower instrument contrast. The FOV of the camera is the angle θ at which the instrument contrast falls below a certain critical value (typically 50% of the contrast on axis).

For an on-axis point detector, analytic estimates can be obtained for the dependence of instrument contrast on the collection solid angle.[9] Numerical simulations are required to estimate the comparatively poorer instrument contrast for off axis detectors. Because the phase variation is proportional to L (the length of the crystal), the contrast degradation also increases with L. Since L determines T_C (the temperature at which the instrument is most sensitive), FOV$\propto\sqrt{T_C}$ since FOV $\sim 1/L$. Furthermore, larger detector elements have smaller instrument contrast.

IV. INCREASING THE FOV

The FOV can be improved by compensating the angular variations of the phase shift. This is achieved by replacing a single birefringent crystal with the optical arrangement shown in Fig. 4. Two crystals each having half the original delay are placed in line with their optic axes mutually perpendicular. A half wave plate placed between the birefringent crystals having its polarization axis at 45, rotates the wave polarized parallel to the fast axis of the first crystal

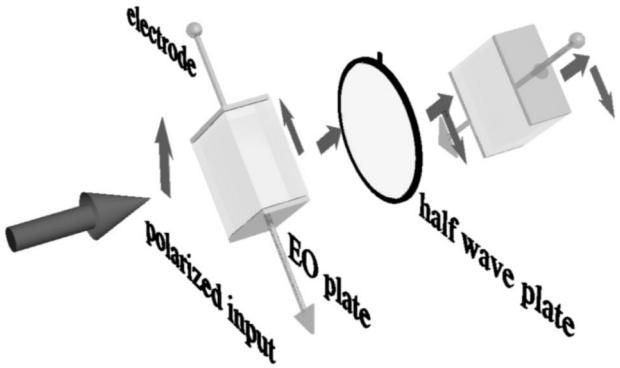

FIG. 4. The optical arrangement for field widening: a 1/2 wave plate in between two birefringent crystals with their optic axes at 90° to each other. The arrows denote polarization states.

onto the fast axis of the second crystal, so that the total birefringent phase shift adds. However, because the phase ''saddle'' is almost invariant under a 90 degree rotation, the angular phase variation of the second crystal almost completely compensates that introduced by the first. The phase variation with angle of each crystal, together with the net phase variation is shown in Fig. 5. The residual phase variation is now approximated by

$$\phi_{\text{wide}}(\theta,\eta)=\phi(\theta,\eta)+\phi(\theta,\eta+90°)$$
$$=2\pi\frac{LB}{\lambda}\left(2+\frac{\sin^2\theta}{2n_0}\left[\frac{1}{n_0}-\frac{1}{n_e}\right]\right). \quad (5)$$

Along the axis $\eta=0$, the ''field widened'' phase variation, $\phi_{\text{wide}}(\theta,\eta)-\phi_{\text{wide}}(0,0)$ is only 4% of that for a nonfield widened system, $\phi(\theta,0)-\phi(0,0)$ (for the same net delay). Because the phase is a weaker function of θ, the contrast improves dramatically.

To demonstrate the effect of field widening, the phase and contrast variation with angle are compared to a nonfield widened system (with better spectral resolution). In Fig. 3, photographs of the angular fringe pattern are shown that illustrate the improvement in phase delay uniformity and improvement in instrument contrast. Observe that in both cases

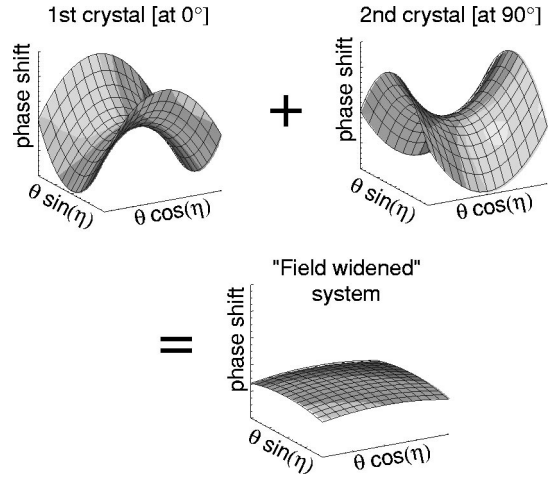

FIG. 5. Schematic illustrating how the field widening works. The phase ''saddle'' of one crystal cancels out the phase saddle of the other crystal.

the contrast at the center is high (~80%). With field widening, the instrument contrast varies only about 5% across all channels of the camera, but decreases by ~70% in the nonfield widened case. For a field-widened system, the main field of view constraints are set by the vignetting of off-axis rays and angular response of the interference filter.

V. CAMERA DESIGN AND INSTALLATION ON H-1NF

In order to maximize the collected light, the camera is placed as close as possible to the plasma. If the angle θ_P subtended by the plasma at the camera is greater than the natural FOV of the interferometer (defined above) then field widening is necessary. Furthermore, we have also chosen to use large aperture (50 mm) optics for all optical components apart from the birefringent crystal, which has a square cross-section aperture 40 mm×40 mm

The focal length of the collimating lens f_1 is chosen equal to the distance between the camera and the center of the plasma. The detector array is placed at the focus of the imaging lens, the focal length of which f_2 is determined by the required system magnification $M=f_1/f_2$. This is set equal to the ratio of width of the plasma cross section X_p to the size of the detector array X_d. Spatial resolution is then X_p/n, where n is the number of detector elements.

The camera installation on H-1NF images a poloidal cross section of the plasma, as shown in Fig. 2. A pair of mirrors internal to the vacuum chamber relay the plasma light to the camera. Although 2D imaging is in principle possible with the camera, the physical obstruction presented by the toroidal magnetic field coils allows only a 1D section view of the plasma to be observed. The total distance along the viewing axis from camera to plasma f_1 is 1550 mm, which is as small as is practically possible. The plasma subtends an angle of approx 6° to the camera. The detector array used is a multianode photomultiplier tube, model A5958 from Hamamatsu, which is a 16 element linear array, each element separated by 1 mm. A 2 mm wide slit aperture is placed over the array, in order to limit the toroidal extent of the viewing region. With $X_D=16$ mm, the required magnification is $M=11.5$, and therefore f_2 must be 135 mm. We have therefore selected a Nikon camera lens, $f=135$ mm and $f/\#=2.8$. An internal blackened viewing dump minimizes the contributions from stray reflections inside the vacuum vessel. The photocurrents are amplified by an array of 16 transimpedance amplifiers of bandwidth 300 kHz prior to digitization. The archived signals are numerically processed using a fast Fourier transform based demodulation algorithm.

Although the imaging optics are fixed by the viewing requirements, the observation wavelength and spectral resolution can be configured by changing the filter and crystal delay.[1,2] The most common configuration on H-1NF is $\lambda=488$ nm (Ar^+), $L=25$ mm (the useful temperature dynamic range is 10–200 eV). At this spectral resolution, the instrument contrast degrades significantly for the outside channels, so that field widening is necessary.

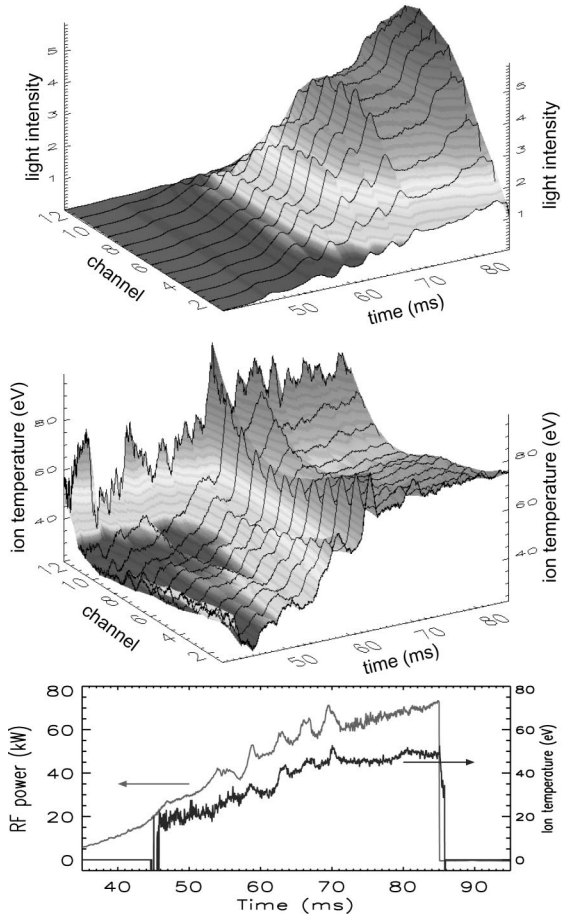

FIG. 6. Light intensity, temperature, and rf power vs time for a power ramp experiment. (A1 ms traveling mean filter has been applied to the light emission and temperature.)

VI. CALIBRATION

For a reliable measurement of the instrument contrast, relative intensity, and phase response of each detector, it is important that the calibration light approximates an extended isotropically radiating source whose subtended solid angle is equal to or greater than that of the plasma. This is achieved by introducing expanded and diffused laser light into the second input port of the first polarizing beam splitter as shown in Fig. 1. Because of the fixed-wavelength, narrow-band spectral nature of laser light, the measured phase and contrast are due only to instrumental effects. When the camera's configuration is changed, a new calibration must be carried out as subtle changes in alignment and position can cause changes in calibration constants (of up to 5%).

VII. RESULTS

Two types of discharges are shown as sample measurements demonstrating the camera's performance.

A. Power ramp experiment

A power ramp experiment is useful to study the dependence of the ion temperature on rf heating power. In this experiment, the application of the approximately linear power ramp follows a 25 ms pulse at full power (~80 kW, 7 MHz, $B=0.15\,\mathrm{T}$) to preionize the plasma. The rf power, temperature, and light intensity are shown in Fig. 6. A 1 ms traveling mean filter has been applied to all but channels 11 and 12, where a 2 and 4 ms mean has been applied, respectively, to improve the signal-to-noise ratio (due to the much weaker light levels in this region). The temperature increases with heating power, and appears to be higher at the edge.

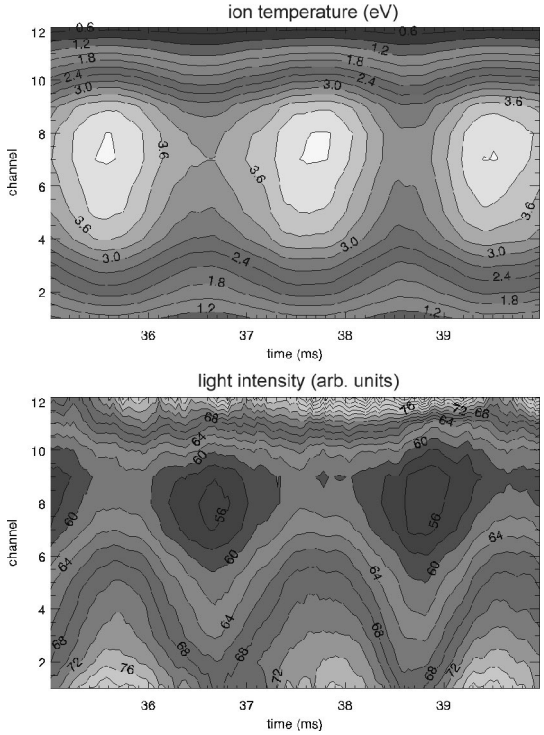

FIG. 7. Light intensity and temperature vs time for a power modulation experiment (the time axis has been expanded to see these fast modulations).

B. Heat modulation experiment

One of the goals in developing this instrument is to study ion transport by examining the spatial profile of modulations in temperature caused by modulations in heating power.[7] Shown in Fig. 7 is the light emission, and temperature for a discharge under the same plasma conditions as above (except that the rf power is modulated at 500 Hz). The time range has been expanded in an interval where the dc component of the plasma parameters are not changing. (A 0.5 ms traveling mean is applied to all channels.) Information about transport can be obtained from the amplitude of T_i variations, and from the rate at which they propagate throughout the plasma.

[1] J. Howard, Rev. Sci. Instrum. **70**, 368 (1999).
[2] J. Howard *et al.* Rev. Sci. Instrum. (these proceedings).
[3] S. Hamberger, B. Blackwell, L. Sharp, and D. Shenton, Fusion Technol. **17**, 123 (1990).
[4] R. Stanley Deans, *The Radon Transform and Some of its Applications* (Krieger, Malabar, FL, 1993).
[5] P. Jacquinot, J. Opt. Soc. Am. **44**, 761 (1954).
[6] P. Jacquinot, Rep. Prog. Phys. **23**, 267 (1960).
[7] N. J. Lopes Cardozo, Plasma Phys. Controlled Fusion **37**, 799 (1995).
[8] J. Howard, J. Opt. Soc. Am. A (submitted).
[9] W. Steel, *Interferometry* (Cambridge University Press, Cambridge, 1967).
[10] A. Yariv, *Optical Electronics* (Saunders College Press, Philadelphia, PA, 1991).